Article

Microwave Plasma-Activated Chemical Vapor Deposition of Nitrogen-Doped Diamond. II: CH₄/N₂/H₂ Plasmas

Benjamin S. Truscott, Mark W. Kelly, Katie J. Potter, and Michael N. R. Ashfold*

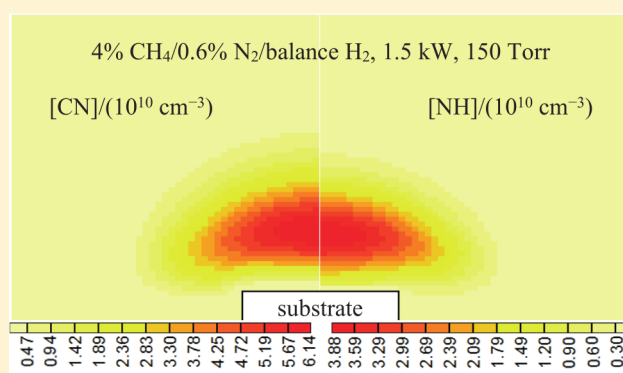School of Chemistry, University of Bristol, Bristol BS8 1TS, U.K.

Yuri A. Mankelevich*

Skobel'tsyn Institute of Nuclear Physics, Moscow State University, Leninskie gory, Moscow 119991, Russia

Institute of Applied Physics, IAP RAS, 46 Ulyanov st., Nizhny Novgorod 603950, Russia

ABSTRACT: We report a combined experimental and modeling study of microwave-activated dilute $CH_4/N_2/H_2$ plasmas, as used for chemical vapor deposition (CVD) of diamond, under very similar conditions to previous studies of CH_4/H_2, $CH_4/H_2/Ar$, and N_2/H_2 gas mixtures. Using cavity ring-down spectroscopy, absolute column densities of $CH(X, v = 0)$, $CN(X, v = 0)$, and $NH(X, v = 0)$ radicals in the hot plasma have been determined as functions of height, z, source gas mixing ratio, total gas pressure, p, and input power, P. Optical emission spectroscopy has been used to investigate, with respect to the same variables, the relative number densities of electronically excited species, namely, H atoms, CH, C_2, CN, and NH radicals and triplet N_2 molecules. The measurements have been reproduced and rationalized from first-principles by 2-D (r, z) coupled kinetic and transport modeling, and comparison between experiment and simulation has afforded a detailed understanding of C/N/H plasma-chemical reactivity and variations with process conditions and with location within the reactor. The experimentally validated simulations have been extended to much lower N_2 input fractions and higher microwave powers than were probed experimentally, providing predictions for the gas-phase chemistry adjacent to the diamond surface and its variation across a wide range of conditions employed in practical diamond-growing CVD processes. The strongly bound N_2 molecule is very resistant to dissociation at the input MW powers and pressures prevailing in typical diamond CVD reactors, but its chemical reactivity is boosted through energy pooling in its lowest-lying (metastable) triplet state and subsequent reactions with H atoms. For a CH_4 input mole fraction of 4%, with N_2 present at 1−6000 ppm, at pressure $p = 150$ Torr, and with applied microwave power $P = 1.5$ kW, the near-substrate gas-phase N atom concentration, $[N]_{ns}$, scales linearly with the N_2 input mole fraction and exceeds the concentrations $[NH]_{ns}$, $[NH_2]_{ns}$, and $[CN]_{ns}$ of other reactive nitrogen-containing species by up to an order of magnitude. The ratio $[N]_{ns}/[CH_3]_{ns}$ scales proportionally with (but is 10^2-10^3 times smaller than) the ratio of the N_2 to CH_4 input mole fractions for the given values of p and P, but $[N]_{ns}/[CN]_{ns}$ decreases (and thus the potential importance of CN in contributing to N-doped diamond growth increases) as p and P increase. Possible insights regarding the well-documented effects of trace N_2 additions on the growth rates and morphologies of diamond films formed by CVD using MW-activated CH_4/H_2 gas mixtures are briefly considered.

The abstract graphic shows: 4% CH₄/0.6% N₂/balance H₂, 1.5 kW, 150 Torr; $[CN]/(10^{10}\ cm^{-3})$ and $[NH]/(10^{10}\ cm^{-3})$; with a "substrate" label and color scale values.

1. INTRODUCTION

Nitrogen is a common impurity in both natural and high-pressure/high-temperature (HPHT) synthetic diamond. In natural diamonds, nitrogen impurities are usually found aggregated in clusters (defined as type Ia diamond), whereas in synthetic HPHT diamonds, nitrogen is typically present at lower overall concentration and located in substitutional sites throughout the lattice (type Ib diamond).[1] Nitrogen is an n-type dopant in diamond, and thus nitrogen-doped diamond has attracted interest as a potential high-electron-mobility semiconductor. Nitrogen is a deep donor,[2] however, and the resulting material has not proved suitable for most electronic applications.

Given the abundance of nitrogen on Earth, it is very challenging to achieve nitrogen-free HPHT diamond growth. Producing such material by chemical vapor deposition (CVD) methods has long been seen as more practicable but still requires great care regarding source gas purity and the minimization of air leaks into the reactor.[3,4] Several previous studies have demonstrated that the presence of trace amounts of nitrogen significantly increases the rate of diamond growth in a microwave

(MW) plasma-activated (PA) CVD process.[5−14] Small nitrogen additions have also been shown to affect the surface morphology,[5,6,14−16] and in particular to encourage the formation of {100}- rather than {111}-faceted surfaces: the former are typically less rough and hence attractive for mechanical applications.[17] Too much nitrogen in the source gas mixture, however, leads to smaller and less-well-oriented surface facets, and a higher sp^2 fraction in the deposited material.[5,18] Another less significant but non-negligible consequence of adding large amounts of N_2 is a reduction in the thermal conductivity of the process gas mixture, which can benefit power coupling efficiency by reducing diffusive transport of heat to the reactor walls.[19]

How nitrogen reacts at the diamond surface and why its presence in the gas phase increases the growth rate and influences the surface morphology is still not fully understood. Various nitrogen-containing species have been proposed as participants in gas−surface reactions contributing to diamond growth. CN radicals have attracted attention based on observed correlations between CN(B → X) emission intensities from the hot plasma region and measured growth rates,[14,20−22] and CN adsorption on a diamond {111} surface has been suggested as a route to nucleating new layer growth.[23] Cao et al.[16] offered a more general view, recognizing possible contributions from a range of gas-phase NH_x and CNH_x species. On the computational front, Larsson and co-workers[24,25] have explored how preadsorbed NH_x ($x = 1, 2$) species might affect gas−surface reactions involving CH_x radicals (which are generally viewed as the dominant C precursor in diamond CVD[26]), and ways in which previously incorporated near-surface substitutional N atoms can influence the energetics, and thus the rates, of the elementary reactions involved in CH_x incorporation.[27,28]

Here, we report spatially resolved absorption and emission measurements of several gas-phase species (H($n = 2, 3$) atoms, NH, CH, CN and C_2 radicals, and triplet N_2 molecules) in MW-activated $CH_4/N_2/H_2$ plasmas operating at pressures (≈150 Torr) and powers (≈1.5 kW) relevant to contemporary MWPACVD processes. The work builds on complementary diagnoses of N_2/H_2 and NH_3/H_2 plasmas presented previously (henceforth paper I[29]), and the experimental measurements are used to inform and tension companion 2-D modeling of the C/N/H plasma chemistry. Similarities and differences between the present model outputs and those from the one previous 2-D simulation of MW activated C/N/H plasmas[30] are highlighted, and possible insights these data provide toward explaining documented effects of trace N_2 additions on the growth rates and morphologies of diamond films formed by CVD using MW-activated CH_4/H_2 gas mixtures are briefly considered.

2. EXPERIMENTS

The MWPACVD reactor, the laser system, and the optical arrangements for the spatially resolved cavity ring down spectroscopy (CRDS) and optical emission spectroscopy (OES) measurements as a function of height (z) above the substrate surface are detailed in paper I[29] or in prior publications cited therein. Table 1 lists the species and transitions probed in the present study.

CRDS was used to determine column densities of electronically excited H($n = 2$) atoms, NH(X), CH(X), and C_2(a) radicals as functions of z, applied microwave power, P, total pressure, p, and gas mixing ratio, as described in previous publications.[29,36,44] The present work also relies on column density measurements of CN(X) radicals, as well as further measurements of CH(X)

Table 1. Probe Transitions Used for Monitoring H*, NH, CH, C_2, CN, and N_2* Species

species	CRDS	OES	[spectroscopic constants]; (A-coefficients)
H*	$n = 3 \leftarrow n = 2$	$n = 3 \rightarrow n = 2$	[31]; (31)
NH	$A^3\Pi \leftarrow X^3\Sigma^-$	$A \rightarrow X$	[32]; (33, 34)
CH	$A^2\Delta \leftarrow X^2\Pi$	$A \rightarrow X$	[35]; (36)
	$B^2\Sigma^- \leftarrow X^2\Pi$		[37]; (38)
C_2	$d^3\Pi_g \leftarrow a^3\Pi_u$	$d \rightarrow a$	[39]; (36)
CN	$B^2\Sigma^+ \leftarrow X^2\Sigma^+$	$B \rightarrow X$	[40]; (41)
N_2*		$C^3\Pi_u \rightarrow B^3\Pi_g$	[42]; (43)

radicals using the $B^2\Sigma^- \leftarrow X^2\Pi$ transition rather than the more traditional A−X system. All of these species, plus electronically excited (triplet) N_2 molecules, were also monitored by OES, using one of two similar optical set-ups.[29,45] H_2, CH_4, and N_2 source gases were supplied via separate, calibrated mass flow controllers and mixed before entering through two diametrically opposed inlets located close below the top of the reactor, situated at an angle of ≈45° to the laser propagation axis. "Base" conditions for these experimental studies were defined as follows: p = 150 Torr, P = 1.5 kW, and input flow rates $F(N_2)$ = 3 standard cm^3 per minute (sccm), $F(CH_4)$ = 20 sccm and $F(H_2)$ = 500 sccm, that is, an $[N]/[C]$ ratio in the input gas mixture of 0.3. When varying one parameter, all others were maintained at their base values unless noted otherwise. The substrate temperature was monitored by two-color optical pyrometry, returning values $T_{sub} \approx$ 1100 K. This source gas mixture represents a much higher N/C ratio than is used in the growth of high-quality CVD diamond but was chosen to allow more detailed study of the gas-phase chemistry of N_2. The experimentally established plasma chemistry informs simulations extended to lower N/C ratios later in the manuscript.

3. EXPERIMENTAL RESULTS

Figure 1a shows a CRD spectrum measured over the wavenumber range 25732−25823 cm^{-1} at z = 8 mm for a $CH_4/N_2/H_2$ plasma operating under base conditions. The spectrum is dominated by the P-branch band head of the CN(B−X) (0,0) transition, but as the accompanying PGOPHER[46] simulation in Figure 1b shows, also displays lines associated with the CH(B−X) (0,0) transition. For completeness, we note a previous CRDS study, in the context of diamond CVD, of CN radicals in an oxyacetylene flame with nitrogen addition,[47] and a study of $CH_4/O_2/N_2$ and $CH_4/NO/O_2/N_2$ flames that exploited this same spectral region.[48] Figure 1c shows an expanded view of a small region of the CRD spectrum centered around 25749 cm^{-1}. This is attractive from a diagnostic perspective because it is free from any contaminating CH(B−X) transitions and includes CN(B−X) (0,0) transitions originating from both high and low J'' levels. As such, it offers a convenient probe of the CN rotational temperature, which, given the operating pressure and prevailing collision frequency and as in our previous analyses of the C_2(d−a) spectra,[44] we regard as diagnostic of the gas temperature ($T_{gas} \approx$ 2900−3000 K) in the region containing the radicals of interest. The CH(B−X) features used for column density measurements are shown in Figure 1a and again on an expanded scale in Figure 1d.

Absolute column densities {M(v = 0)} (where M = C_2, CH, CN, or NH) can be derived from such spectra using
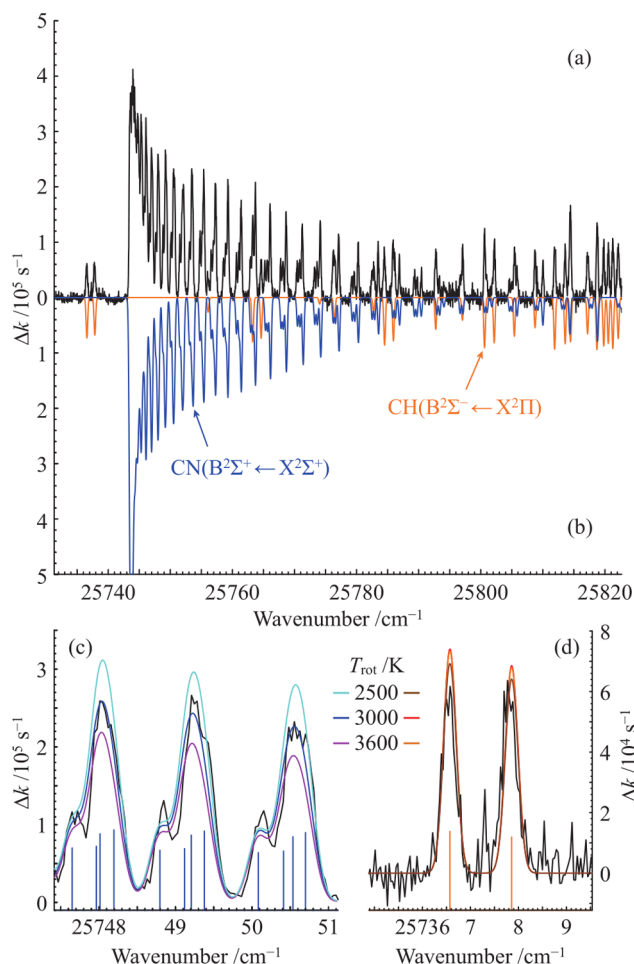
Figure 1. Part of the CN(B–X) and CH(B–X) $\Delta\nu = 0$ systems (a) as measured by CRDS at $z = 8$ mm in a $CH_4/N_2/H_2$ plasma operating under base conditions along with (b) a PGOPHER simulation that assumes $T_{rot} = 3000$ K and serves to illustrate lines associated with the different carriers. Expanded views of the spectral regions used for monitoring CN(X) and CH(X) column densities are shown in panels c and d, respectively, along with accompanying PGOPHER simulations that illustrate the spectral sensitivity to T_{rot} and, by inference, T_{gas}, in the case of the CN(B–X) lines. The CH(B–X) features, in contrast, depend only weakly on temperature.

$$\{M(\nu = 0)\} = \frac{8\pi L \bar{\nu}^2}{A p_{line}} \frac{g_l}{g_u} \int_{line} \Delta k \, d\bar{\nu} \qquad (1)$$

where L is the length of the cavity (here, 92 cm), g_l and g_u are the degeneracies of the lower and upper states involved in the respective transitions, A is the Einstein A-coefficient for the $\nu' = 0$ to $\nu'' = 0$ transition, Δk is the measured change in ring-down rate (in s^{-1}) at a given wavenumber ($\bar{\nu}$, in cm^{-1}), and p_{line} is the ratio of the integrated intensity of the spectral line under study to the total (0,0) band intensity, which can be calculated using PGOPHER and the relevant spectroscopic constants (Table 1) if the radical is localized in a region of reasonably constant T_{gas}. Degeneracies, Einstein A-coefficients, and favorable lines for probing C_2, CH (via the A–X transition), NH radicals, and H($n = 2$) atoms by CRDS have been detailed in previous publications.[29,36,44] The corresponding quantities used for the CN(B–X) transition are $g_l = g_u = 2$ and $A = 1.48 \times 10^7$ s^{-1} (ref 41) and, for the CH(B–X) transition, $g_l = 4$, $g_u = 2$ and $A = 2.80 \times 10^6$ s^{-1} (ref 38). The present analyses assume $p_{line} = (6.27 \pm 0.45)$

$\times 10^{-3}$ for the $P_1(18.5)$ line of the CN(B–X) (0,0) band at 25750.70 cm^{-1} and $p_{line} = (6.56 \pm 0.16) \times 10^{-3}$ for the $R_1(13.5)$ line of the CH(B–X) (0,0) band at 25736.53 cm^{-1}, where the uncertainty in the effective T_{gas} along the column determines the quoted uncertainties in p_{line} on the basis that $T_{gas} = 2900 \pm 300$ K. To reduce the influence of baseline variations and other interferences, the CRDS spectra were fitted with respect to the intensities of these lines within the groups of near-lying lines shown in Figure 1c,d, accounting for their known relative intensities and the temperature dependences thereof, rather than to the lines individually. To convert the experimental $\{M(\nu = 0)\}$ values to total column densities (sums over all vibrational states) requires multiplication by the appropriate vibrational partition functions: namely, 1.83 for $C_2(a)$, 1.36 for CH, 1.58 for CN, and 1.28 for NH, all calculated assuming $T_{vib} = T_{gas} = 2900$ K.

The more obvious differences between optical emission spectra from MW-activated $CH_4/N_2/H_2$ and CH_4/H_2 plasmas are in the near-UV region, where the former shows features attributable to some or all of CN*, N_2*, or NH*, depending on the relative N and C fractions. The H*, C_2*, and CH* emissions, in contrast, show no obvious changes upon addition of small $F(N_2)$ to a CH_4/H_2 plasma. The dependence of the near-UV (324–360 nm) part of the optical emission spectrum on the C/N ratio is illustrated in Figure 2a, which compares spectra of MW-activated gas mixtures comprising 3 sccm N_2 and, respectively, 0, 3, and 10 sccm CH_4 along with 500 sccm of H_2, all operating at base input power and pressure. As Figure 2b shows, increasing
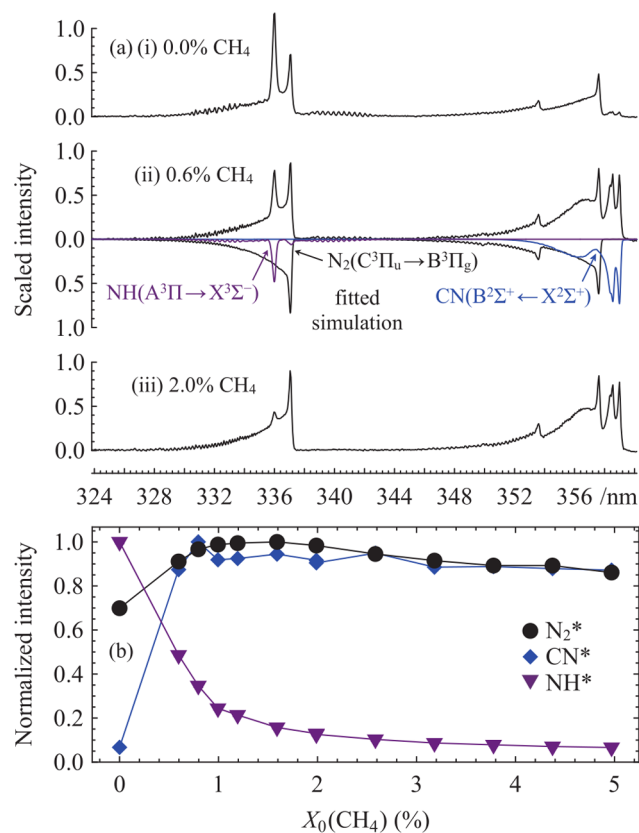
Figure 2. (a) Optical emission spectra, measured at $z = 7$ mm, of MW activated gas mixtures comprising 3 sccm N_2 and, respectively, (i) 0, (ii) 3, and (iii) 10 sccm CH_4 along with 500 sccm of H_2, operating at base input power and pressure. (b) Plot illustrating the variation in relative CN*, N_2*, and NH* emission intensities with increasing $F(CH_4)$, with the maximum intensity of each emission normalized to unity.

$F(CH_4)$ leads to a strong initial increase in CN* emission and a progressive decrease in the NH* emission, while the N_2* emission intensity is relatively insensitive to changing $F(CH_4)$.

Figure 3a shows z-profiles of the C_2(d−a), H($n = 4 \rightarrow n = 2$), and CH(A−X) emission intensities from a $CH_4/N_2/H_2$ plasma
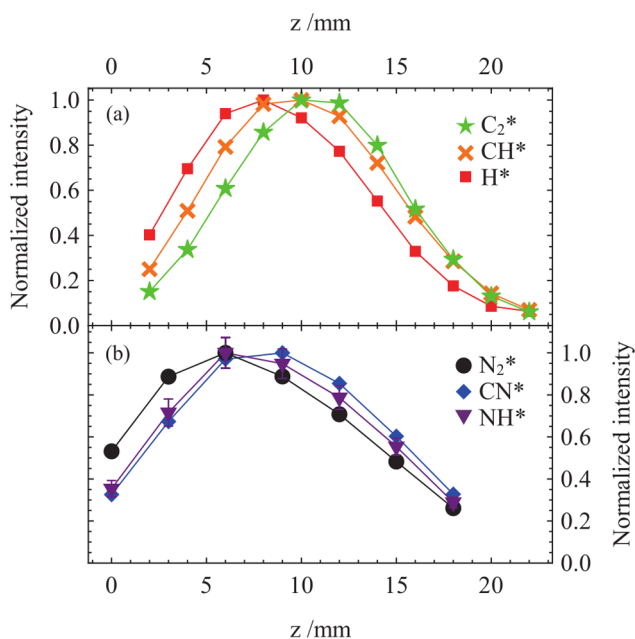
Figure 3. z-profiles of (a) the C_2(d−a), H($n = 4 \rightarrow n = 2$) and CH(A−X) emission intensities and (b) the N_2(C−B), NH(A−X), and CN(B−X) emissions from a $CH_4/N_2/H_2$ plasma operating under base conditions measured using the two complementary optical set-ups summarized in the text.

operating under base conditions measured using the earlier optical setup.[45] Figure 3b shows profiles for the N_2(C−B), NH(A−X), and CN(B−X) emissions, obtained using the more sensitive optical telescope arrangement described in paper I[29] because of the relatively weak near-UV emission. The spatial resolutions obtained with these two set-ups are estimated as ∼0.5 and ∼3 mm, respectively. Each profile is normalized such that the peak emission intensity is unity. The distributions shown in Figure 3a match those reported previously for the same species in a MW-activated CH_4/H_2 gas mixture operating under very similar conditions in this same reactor.[45] As in the N_2/H_2 plasma,[29] the N_2* emission profile peaks at low z, lower than that of the H* emission. The NH* profile also peaks at low z, below the emission maxima of any of the C-containing species, and is less spatially extensive in the $CH_4/N_2/H_2$ plasma than in a CH_4-free N_2/H_2 plasma. The CN* emission profile maximizes at slightly larger z and is similar in shape to the CH* emission.

From here on, we recognize that the C_2*, CH*, and H* emissions (and, as shown below, the absolute column densities and spatial profiles of these species as determined by CRDS) are changed little by small additions of N_2 and focus on the possible diagnostic value of the NH*, N_2*, and CN* emissions and their variations with process conditions. Figure 4a, for example, shows the variation in the respective emission intensities with increasing MW power. Trebling P from 0.6 to 1.8 kW results in an approximately 2-fold increase in the N_2* emission intensity (measured at z = 7 mm), similar to that observed in a pure N_2/H_2 plasma operating in the same reactor and primarily attributable to an increase in plasma volume.[29] The NH* and CN* emission
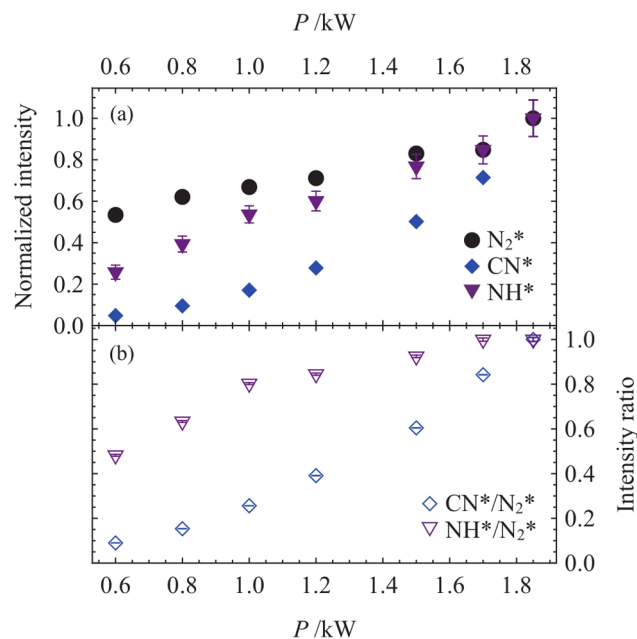
Figure 4. (a) NH*, N_2*, and CN* emission intensities measured at z = 7 mm ($CH_4/N_2/H_2$ 20/3/500 sccm plasma) as a function of applied MW power under otherwise base conditions. The emission intensities of each species are normalized to the maximal value measured at any P. The P-dependence of the NH*/N_2* and CN*/N_2* intensity ratios are shown in panel b.

intensities show much steeper P-dependences, increasing by factors of ≈4 and ≈15, respectively. These differences are emphasized by the NH*/N_2* and CN*/N_2* intensity ratio plots shown in Figure 4b, wherein N_2 (by virtue of its comparative unreactivity) is essentially acting as an actinometer. As discussed alongside the C/N/H plasma modeling (section 4, below), the greater increases in the NH* and, particularly, CN* emission intensities can be understood in terms of the small P-induced increase in the maximal gas temperature, since a concomitant increase in the H atom density in the hot plasma region accelerates the chemistry responsible for forming these species.

Absorption (CRDS) measurements return absolute column densities and thus provide a more direct measure of the effects of changes in process condition. Figure 5 shows z-dependent profiles of {NH($v = 0$)} measured using the NH(A−X) lines detailed in paper I,[29] of {CN($v = 0$)} and {CH($v = 0$)} measured using the CN(B−X) and CH(B−X) lines shown in Figure 1c,d, and of {CH($v = 0$)} measured using CH(A−X) lines, as previously,[44] with an assumption in all cases that $T_{rot} = 2900 \pm 300$ K. We recognize that this is likely to be an overestimate of T_{gas} at the lowest z value (2 mm) for which we report data, but using NH as an example, even if the effective T_{gas} is as low as 2200 K, the {NH($v'' = 0$)} value plotted in Figure 5 would only need to be increased by a factor of 1.1 (i.e., ∼10%). The {CN($v = 0$)} and {CH($v = 0$)} data were both determined under base conditions of 20/3/500 sccm $CH_4/N_2/H_2$ flow rates, p = 150 Torr, and P = 1.5 kW. As Figure 6 will show, {NH($v = 0$)} declines greatly with increasing $F(CH_4)$; the z-profile for {NH($v = 0$)} shown in Figure 5 was thus measured with a CH_4-lean, N_2-rich, 2/15/500 sccm input mixture. As Figure 5 also shows, the {CH($v = 0$)} values obtained from analysis of the B−X lines shown in Figure 1d agree well with those derived using the same CH(A−X) lines as in our previous studies of C/H plasmas, though we note that both are slightly (≈10%) lower than had been measured in this
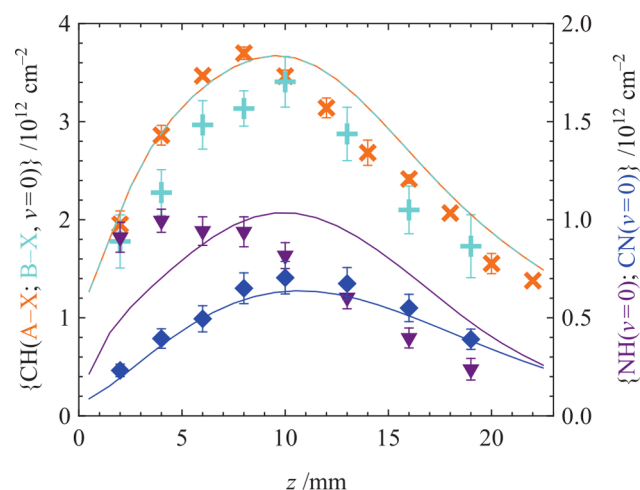
**Figure 5.** Profiles of $\{NH(v=0)\}$, $\{CN(v=0)\}$, and $\{CH(v=0)\}$ as a function of z, obtained by CRDS probing of $CH_4/N_2/H_2$ plasmas operating with respective flow rates of 2/15/500 sccm (for NH) and 20/3/500 sccm (for CN and CH) and base values of total pressure and applied power. Note the good agreement in the $\{CH(v=0)\}$ values determined when monitoring via the two different electronic transitions. The solid curves through these data show the z-dependent column densities of these three species returned by the modeling described in section 4. Note that the calculated $\{CN(v=0)\}$ values have been increased by a factor of 3.5 prior to display.

same reactor under nominally identical process conditions in 2008.[44] Compared with $\{CN(v=0)\}$ and $\{CH(v=0)\}$, $\{NH(v=0)\}$ peaks lower, at $z \approx 4-5$ mm, and declines gently with increasing z. Relative to the CH_4-free N_2/H_2 plasma,[29] the absolute magnitude of $\{NH(v=0)\}$ measured at $z \approx 4-5$ mm is similar (although $F(N_2)$ is 2.5 times greater in the present experiments), and the decline to higher z is steeper, mimicking the spatial distribution of NH* emission shown in Figure 3b.

Figure 6a illustrates the contrasting dependencies of these three species (measured at $z = 8$ mm) upon introducing progressively greater $F(CH_4)$ to a pre-existing N_2/H_2 plasma operating at base power and pressure. Again, the $\{CH(v=0)\}$ and $\{CN(v=0)\}$ data were both recorded using $F(N_2) = 3$ sccm, whereas to increase signal levels, the $\{NH(v=0)\}$ data were recorded at $F(N_2) = 15$ sccm. $\{CH(v=0)\}$ is seen to exhibit the same $X_0(CH_4)^{0.5}$ dependence as found previously in the case of (N_2-free) CH_4/H_2 plasmas, where $X_0(CH_4)$ is the CH_4 input mole fraction.[44,49] $\{CN(v=0)\}$ shows a similar initial rise upon adding CH_4, but plateaus at $F(CH_4) \approx 2.5$ sccm under the prevailing plasma conditions, while $\{NH(v=0)\}$ declines as $X_0(CH_4)^{-0.5}$. The corresponding trends for $\{CH(v=0)\}$ and $\{CN(v=0)\}$ upon adding N_2 to a pre-existing $F(CH_4)/F(H_2) = 20/500$ sccm plasma operating at base power and pressure are shown in Figure 6b. The former shows a modest ($\approx$33%) increase as $F(N_2)$ is increased to $\approx$1.5 sccm, while $\{CN(v=0)\}$ scales almost proportionally with $0 \leq F(N_2) \leq 7$ sccm.

Figure 7 shows the measured (at $z = 8$ mm) variations in $\{CH(v=0)\}$, $\{NH(v=0)\}$, and $\{CN(v=0)\}$ as a function of applied MW power. Again, practical considerations dictated that the $\{CH(v=0)\}$ and $\{CN(v=0)\}$ data were both recorded for base conditions with $F(CH_4)/F(N_2)/F(H_2) = 20/3/500$ sccm while the $\{NH(v=0)\}$ data were obtained using modified flow rates of 2/15/500 sccm. $\{CH(v=0)\}$ is seen to increase near-linearly with P over the range 0.75$-$1.85 kW, as observed previously when using (nominally) N_2-free C/H plasmas.[44] $\{NH(v=0)\}$ shows a similar P-dependence to $\{CH(v=0)\}$ in
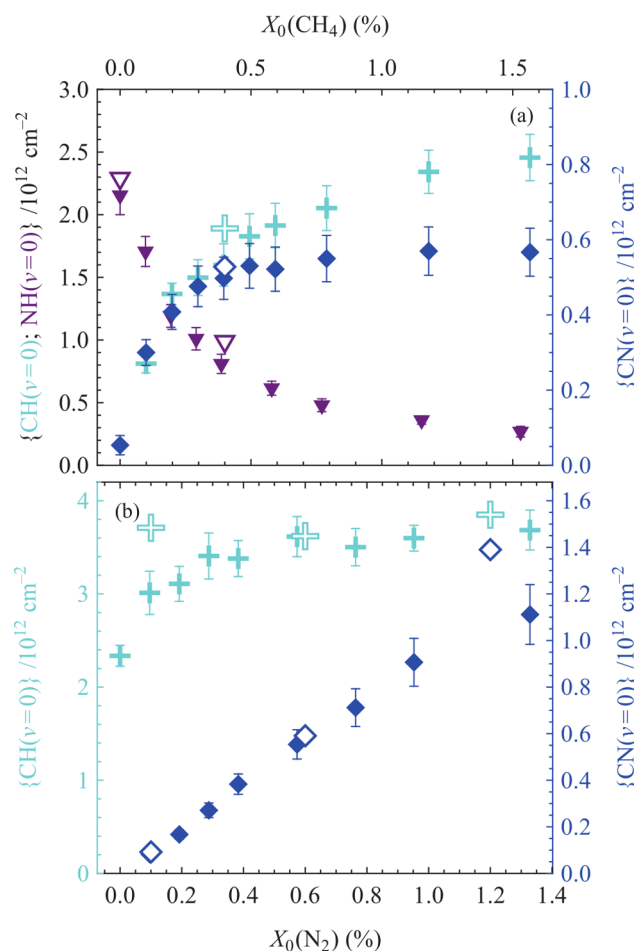
Figure 6. Solid points show the measured variations in (a) $\{CH(v=0)\}$, $\{CN(v=0)\}$, and $\{NH(v=0)\}$ following addition of CH_4 to pre-existing N_2/H_2 plasmas (3/500 sccm when probing CH and CN, 15/500 when monitoring NH) and (b) $\{CH(v=0)\}$ and $\{CN(v=0)\}$ upon adding N_2 to a pre-existing CH_4/H_2 (20/500 sccm) plasma. All measurements were made at $z = 8$ mm, and all plasmas were operating at base power and pressure. The corresponding quantities returned by the model calculations described in section 4 are indicated by open symbols. As in Figure 5, the calculated $\{CN(v=0)\}$ values have been increased by a factor of 3.5 prior to display.

this $CH_4/N_2/H_2$ plasma and to $\{NH(v=0)\}$ measured in the CH_4-free N_2/H_2 plasma.[29] Comparing the absolute magnitudes of $\{NH(v=0)\}$ measured in the $CH_4/N_2/H_2$ and N_2/H_2 plasmas at any given P, however, we again see that the $\{NH(v=0)\}$ values measured in the $CH_4/N_2/H_2$ plasma at $z = 8$ mm (Figure 7) are only $\approx$40% those measured in the N_2/H_2 plasma, even though $F(N_2)$ was 2.5 times higher and $F(CH_4)$ was only 2 sccm. $\{CN(v=0)\}$ shows the steepest P-dependence, increasing more than 10-fold over the measured range.

$\{CN(v=0)\}$ also shows greater sensitivity to total pressure than $\{CH(v=0)\}$. Figure 8 depicts data for two very different N/C input ratio ranges. As Figure 8a shows, $\{CN(v=0)\}$ and $\{CH(v=0)\}$ (monitored via the B$-$X transition and color coded accordingly), measured under base conditions at $z = 8$ mm, both scale with p across the range 75$-$200 Torr. $\{CN(v=0)\}$ is a tenth of $\{CH(v=0)\}$ at 75 Torr but has a steeper rate of increase with p and approaches one-fifth of $\{CH(v=0)\}$ at 200 Torr. Figure 8b shows data recorded under rather different conditions, closer to those used in practical CVD diamond growth, and over a wider range of p. Again, the measurements were made at $z = 8$ mm and
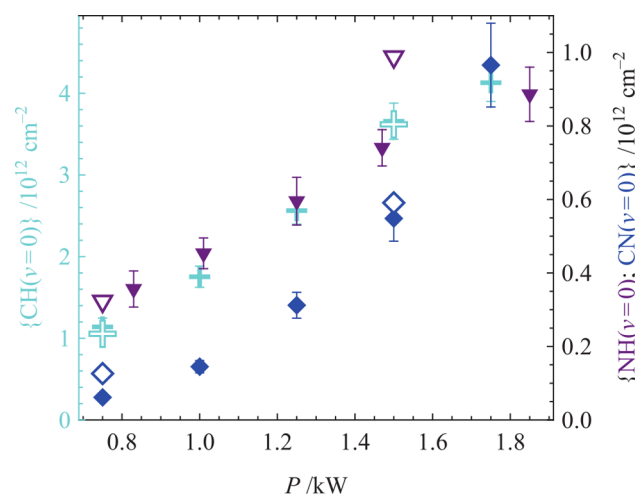
Figure 7. Solid points show measured variations in $\{CH(v = 0)\}$, $\{NH(v = 0)\}$, and $\{CN(v = 0)\}$ with increasing MW power for plasmas formed using $CH_4/N_2/H_2$ flow rates of 20/3/500 sccm (for CH and CN) and 2/15/500 sccm (for NH). All measurements were made at $z = 8$ mm. The corresponding quantities returned by the model calculations described in section 4 are indicated by open symbols. As in Figure 5, the calculated $\{CN(v = 0)\}$ values have been increased by a factor of 3.5 prior to display.

with $F(CH_4) = 20$ sccm (in a total flow rate of 500 sccm). The incident MW power was higher ($P = 1.8$ kW), but the most significant difference was a much lower $F(N_2)$, equivalent to 0.1 sccm or 200 ppm, introduced as 10 sccm of a 1% N_2 in H_2 mixture. Again, $\{CN(v = 0)\}$ is very much smaller than $\{CH(v = 0)\}$ (here monitored via the A–X transition) at low p (120 Torr), but $\{CN(v = 0)\}$ increases much more steeply, such that at $p = 300$ Torr, the measured $\{CN(v = 0)\}/\{CH(v = 0)\}$ ratio has increased to ≈ 0.1.

As in paper I,[29] all of the measured trends are now discussed and interpreted in light of companion modeling studies of the prevailing plasma chemistry and composition.

4. C/N/H PLASMA MODELING

The 2-D (r, z) model used in the present C/N/H plasma modeling draws on previously reported plasma-chemical mechanisms for the two-component N/H and C/H gas mixtures.[29,49] To these are added a C/N/H chemical mechanism for neutral species, H, H_2, CH_x ($x = 0$–4), C_2H_y ($y = 0$–6), C_3H_x ($x = 0$–2), C_4H_x ($x = 0$–2), NH_x ($x = 0$–3), N_2, and H_xCN ($x = 0$–2),[49–52] and kinetic data for C/N coupling, H-shifting, and thermal decomposition reactions involving the additional species H_2CNH, H_3CNH, and H_3CNH_2.[53] Also considered were the reaction kinetics of electrons in different C/N/H mixtures,[29,49,54,55] for electron–ion recombination reactions, and ion interconversion reactions involving H_2^+, H_3^+, $C_2H_2^+$, $C_2H_3^+$, N_2H^+, NH_4^+, and $HCNH^+$.[56] The most important of the N_2 dissociation reactions and C/N coupling reactions are listed in Table 2, but the full base reaction mechanism involved 45 species and ≈ 350 direct and reverse reactions. The effects of adding a few further species (e.g., HCCN, NCCN, CH_2CNH, and CH_3CN) were probed, but none were found to have any serious consequence and thus were ultimately omitted. All of the important plasma-chemical conversions identified in the C/H and N/H plasma modeling studies still play significant roles in the C/N/H plasma, but since these have been elaborated previously,[29,49] we henceforth concentrate particularly on C/N
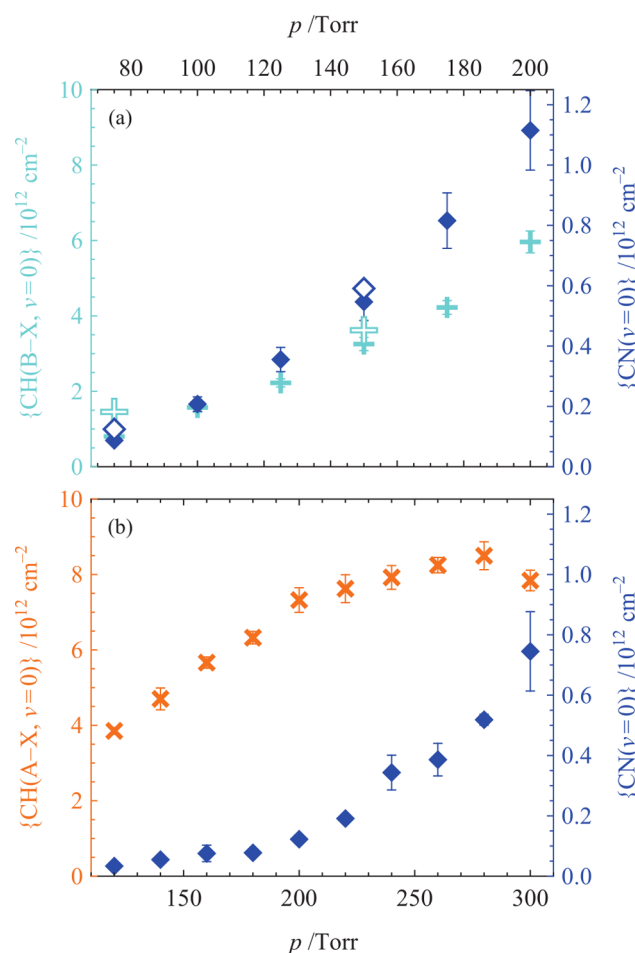
Figure 8. Measured variations in $\{CH(v = 0)\}$ and $\{CN(v = 0)\}$ as a function of total gas pressure measured (a) under base conditions, over the range 75–200 Torr, and (b) at $P = 1.8$ kW with $F(CH_4) = 20$ sccm and an effective $F(N_2) = 0.1$ sccm (in a total flow rate of 500 sccm) over the range $120 \leq p \leq 300$ Torr. All measurements were made at $z = 8$ mm. The corresponding quantities returned by the model calculations described in section 4 are shown by open symbols in panel a. As in Figure 5, the calculated $\{CN(v = 0)\}$ values have been increased by a factor of 3.5 prior to display.

Table 2. Most Important N_2 Dissociation and C/N Coupling Reactions Included in the Present Study with T-Dependent Rate Coefficients k (cm^3 mol^{-1} s^{-1})[a]

reaction	rate coefficient $k = AT^b \exp(-E/RT)$			
	A	b	E	ref
$N_2(A3) + H \rightleftharpoons NH + N$	1.2×10^{12}	0	3850	29
$CH_3 + N \rightleftharpoons H_2CN + H$	6.10×10^{14}	-0.31	290	50
$CH_3 + N \rightleftharpoons HCN + H_2$	3.70×10^{12}	0.15	-90	50
$CH_3 + NH \rightleftharpoons H_2CNH + H$	4.00×10^{13}	0	0	52
$CH + N_2 \rightleftharpoons HCN + N$	3.12×10^9	0.88	20130	50
$C + N_2 \rightleftharpoons CN + N$	6.30×10^{13}	0	46020	50
$CN + H_2 \rightleftharpoons HCN + H$	2.95×10^5	2.45	2240	50
$H + H_2CN \rightleftharpoons HCN + H_2$	7.80×10^{13}	0	0	51

[a]Units: cal, cm, s, $R = 1.9873$ cal (mol K)$^{-1}$. $N_2(A3)$ represents the metastable $A^3\Sigma_u^+$ state (the lowest-energy triplet state) of N_2, and the gas temperature T is quoted in K.

coupling effects. "Base" conditions for the calculations were the same as in the experiments except that the modeling assumes

F_{total} = 500 sccm, i.e., $F(H_2)$ = 477 sccm rather than the 500 sccm used in most of the experiments.

4.1. Plasma-Chemical Conversions in C/N/H Plasmas. Modeling the Effects of Adding CH₄ to a N/H Plasma. Important findings from our previous investigations of C/H plasmas include that (i) the absorbed MW power is expended mainly on gas heating, via rotational and vibrational excitation of H_2, (ii) there is rapid redistribution within the CH_x and C_2H_y groups as a result of fast H-shifting reactions, and (iii) there exist three characteristic regions within the reactor volume, distinguished by the prevailing C_xH_y interconversion reactions.[44,49] A key result of our analyses of MW-activated N/H plasmas[29] was that the dominant N_2 decomposition mechanism in an N_2/H_2 plasma involves formation of various N_2^* states by electron impact excitation, the radiative or collisional relaxation of which results in an overpopulation (relative to local thermodynamic equilibrium) of the lowest, metastable $A^3\Sigma_u^+$ triplet state, henceforth abbreviated as $N_2(A3)$. That is,

$$N_2 + e \rightarrow N_2(A3) + e \tag{2}$$
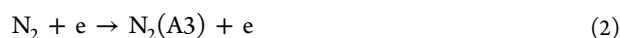
which can be followed by reaction with H atoms:

$$N_2(A3) + H \rightarrow NH + N \tag{3}$$

In the case of C/N/H plasmas, this source is complemented by reaction 4, which was assumed to be the dominant source of N atoms in the one previous modeling study of a MW-activated C/N/H plasma:[30]
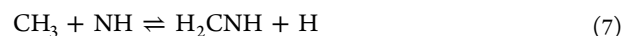
$$CH + N_2 \rightleftharpoons HCN + N \tag{4}$$

Reaction 4 is only mildly endothermic ($\Delta_r H < 0.2$ eV), with a calculated maximal rate $R_4 \approx 1.6 \times 10^{14}$ cm^{-3} s^{-1} in the hot plasma center under the present base conditions. As such, it is of comparable importance to reaction 3 as a source of N and NH species in the plasma core, and its impact extends further into the cooler regions. Integrating over the whole reactor volume, reaction 4, rather than reaction 3, is calculated to make the greater contribution to N atom production for $p \geq 150$ Torr and input methane fractions ≥4%. R_4 drops sharply with decreasing p (e.g., maximal $R_4 \approx 3 \times 10^{13}$ cm^{-3} s^{-1} at $p = 75$ Torr) due to the fall of both $[N_2]$ and $[CH]$, while the maximal rates of reaction 3 only vary by ≈30% upon decreasing p from 150 to 75 Torr. This latter result can be explained by recognizing that the ≈3-fold decrease in $[H]$ upon decreasing p from 150 to 75 Torr is compensated by a corresponding increase in $[N_2(A3)]$ as a result of its reduced quenching by H and H_2. Reaction 5,

$$C + N_2 \rightleftharpoons CN + N \tag{5}$$

is more strongly endothermic ($\Delta_r H \approx 2$ eV) and its calculated rate is correspondingly lower than (namely, around a quarter) that of reaction 4 under base conditions in the hot plasma region.

Reactions 4 and 5 contribute also to H_xCN ($x = 0, 1$) production, but as in our previous modeling of C/N/H gas mixtures in a hot filament CVD reactor,[51] the present analysis reveals other, more important, sources within the family of reactions involving the H_yCNH_z ($y = 0$–2 for $z = 0$, and $y = 2$ for $z = 1$) group. The observed decrease in {NH($v = 0$)} upon CH₄ addition (recall Figure 6b) is one indicator of a family of reactions between NH_x and CH_x ($x = 0$–3) radicals that, taken together, are an important source of H_yCNH_z species. Of this set, reactions 6–8 involving CH_3 radicals predominate under the present conditions:

$$CH_3 + N \rightleftharpoons H_2CN + H \tag{6}$$

$$CH_3 + NH \rightleftharpoons H_2CNH + H \tag{7}$$

$$CH_3 + N \rightleftharpoons HCN + H_2 \tag{8}$$

Other members of the family, for example, $CH_2 + N \rightleftharpoons HCN + H$ and $CH + NH_3 \rightleftharpoons H_2CNH + H$, make lesser contributions. The NH_x and H_yCNH_z species are processed further, by thermal decomposition and through their participation in fast H-shifting reactions, in favor of NH_3 and HCN (which is the most stable CN-containing species in the present environment). That said, N_2 remains the dominant N-containing species, as in the MW-activated N_2/H_2 and NH_3/H_2 mixtures.[29] For the base C/N/H gas mixture, the present calculations suggest that N_2 constitutes >99.75% of the total nitrogen content within the reactor and ≈99.5% of the nitrogen content even in the hot plasma region. HCN accounts for ≲0.25% of the nitrogen content in the entire reactor; the total NH_3 content is roughly 2 orders of magnitude further less; and the fractions of all other N-containing species included in the model are orders of magnitude lower still.

Figure 9 shows the spatial distributions of the CN and NH radical number densities, [CN] and [NH], returned by the 2-D
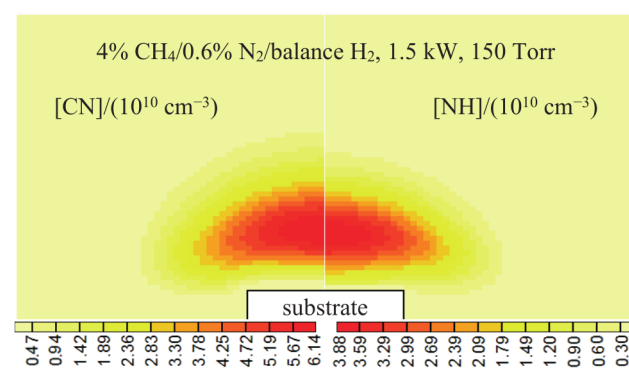
Figure 9. Two-dimensional (r, z) plots showing the predicted total number densities of CN and NH radicals in a 4%CH₄/0.6%N₂/H₂ plasma, total flow rate $F = 500$ sccm, $P = 1.5$ kW, and $p = 150$ Torr. The model assumes cylindrical symmetry, a substrate diameter of 3 cm, and a reactor radius, $r = 6$ cm, and height, $h = 6.2$ cm.

model for base conditions. The observed localization is consistent with the combined effects of primary production of CN and NH_x radicals in the hot plasma region, the above-mentioned species interconversions, and diffusional and thermodiffusional transfer of both radical and stable species. The calculated $[CH](r, z)$ distribution is very similar to that of [CN], and thus not shown; the calculated forms of the [CH] and $[C_2]$ distributions are also very similar to those reported in our earlier modeling of MW-activated C/H plasmas.[49] The predicted localization of these radical species within the hot plasma region is fully consistent with the T_{rot} values returned by the corresponding CRDS measurements (Figure 1) and the z-profiles shown in Figures 3 and 5.

The predicted (r, z) distributions of $[N_2]$, $[N]$, and $[NH_3]$ are each similar to the corresponding distributions in an N_2/H_2 plasma[29] and so are not repeated here. The present calculations show HCN distributed throughout the whole reactor volume, despite its production being concentrated in the hot plasma region, with a mole fraction distribution that maximizes in the cold (near-wall) regions as a result of thermodiffusional transfer. In contrast to the radical species featured in Figure 9, for which the production and loss terms tend to be in local balance, the HCN distribution is determined by the balance between the

production reactions outlined above and the outflow of HCN from the reactor.

We now consider the spatial distribution and the absolute values of the CN concentration in detail. The [CN] spatial distribution is determined by the product of [HCN] and the [H]/[H$_2$] ratio as a result of the fast equilibration reaction

$$CN + H_2 \rightleftharpoons HCN + H \tag{9}$$

The forward reaction is exothermic ($\Delta_r H \approx -1.3$ eV), and the excess energy is preferentially partitioned into HCN product vibration, particularly the C−H stretch mode (ν_3).[57] The rates of the forward (R_{+9}) and reverse (R_{-9}) reactions in the hot plasma region under base conditions are both calculated to be $\approx 2.5 \times 10^{18}$ cm^{-3} s^{-1}. These rates are higher than the vibrational−translational (V−T) relaxation rate of HCN($v > 0$) molecules through collision with H$_2$, C$_2$H$_2$ or HCN,[58] and could be comparable with the (unknown) rate of V−T relaxation through collision with H atoms. The measured CN column densities shown in Figures 5−7 are all ≈ 3.5 times those simulated on the basis of vibrational−translational equilibrium: this implies, in particular, the assumption that the vibrational temperature $T_{vib}(\text{HCN}, \nu_3) = T_{gas}$. However, given the rapidity of reaction 9 relative to likely relaxation processes, we cannot exclude the possibility that $T_{vib}(\text{HCN}, \nu_3) \gg T_{gas}$. Thus, while the 3.5-fold discrepancy could be due to imperfections in the assumed reaction mechanisms and/or temperature-dependent rate coefficients, given the quantitative accuracy with which the density distributions of the other species are reproduced, it could also be explained in a more restricted and physically motivated sense. Assigning an enhanced rate constant for HCN($\nu_3 > 0$) molecules in the endothermic reaction (−9) would have the required effect of increasing the steady-state CN concentration by some factor b. As Figures 5−7 show, the experimental and model {CN($v = 0$)} values are in excellent accord if we take $b \approx 3.5$.

A square-root dependence, {CH($v = 0$)} $\sim F(\text{CH}_4)^{0.5}$, reminiscent of that shown in Figure 6a, was observed and explained previously for C/H plasmas.[49] {CN($v = 0$)} in the present C/N/H plasmas shows a similar $F(\text{CH}_4)^{0.5}$ dependence for $F(\text{CH}_4) < 0.5 \times F(\text{N}_2)$ but saturates for $F(\text{CH}_4) \approx F(\text{N}_2)$, whereas {NH($v = 0$)} varies as $F(\text{CH}_4)^{-0.5}$ while N$_2$ is in excess. As Figure 6a shows, the present 2-D modeling reproduces all of these trends and dependences well. The saturation in {CN($v = 0$)} with increasing $F(\text{CH}_4)$, and thus increasing [CH$_x$] ($x = 0−3$), reflects the concomitant reduction in [NH$_x$] ($x = 0−2$) due to reactions 6−8 and the saturation of H$_y$CNH$_z$ sources.

The dominant ions in the plasma also change upon CH$_4$ addition. The most abundant ions in the base N/H plasma considered in paper I are NH$_4^+$ and N$_2$H$^+$,[29] whereas the present calculations identify the most abundant ions in the base C/N/H plasma as C$_2$H$_2^+$ and C$_2$H$_3^+$, as in a C/H plasma, but supplemented by HCNH$^+$ and NH$_4^+$. Other more complex H$_x$C$_y$N$_z^+$ ions are not included in the reaction scheme as we assume them to be decomposed effectively in the hot plasma region.

4.2. Effects of Varying the Applied Microwave Power and the Total Pressure. The consequences of varying power and pressure on N/H and C/N/H plasmas are deduced to be very similar. As for the N/H plasma,[29] the observed variations with increasing P can be explained in terms of a progressive increase in the plasma volume ($V_{pl} \sim P$, with $V_{pl} \approx 70$ cm^3 under base conditions, giving a spatially averaged power density, $Q \approx 21.5$ W cm^{-3}) while maintaining a broadly constant $T_e \approx 1.25$ eV

at the plasma center. The 2-D modeling shows the maximum gas temperature, T_{max}, increasing by $\approx 4\%$ (from 2770 to 2890 K) as P is increased from 750 to 1500 W. As Figure 7 shows, the predicted variations in {CH($v = 0$)}, {CN($v = 0$)}, and {NH($v = 0$)} match the measured trends well.

Modeling also shows that decreasing p at constant P is accommodated by a modest (less than proportional to the pressure drop) increase in the plasma volume, V_{pl}, while maintaining n_e broadly constant and with a minor increase in the electron temperature: T_e increases $\approx 10\%$ upon decreasing p from 150 to 75 Torr. The 2-D model succeeds in capturing all of the observed p-dependent trends in the species column densities, as shown in Figure 8a. As with the N/H plasma,[29] the z-dependent {NH($v = 0$)} profile (shown in Figure 5 for the case of $p = 150$ Torr only) is shown by both experiment and modeling to become flatter at lower pressure.

The measured {CN($v = 0$)} column densities and CN* emission intensities both increase more steeply with increasing P or p than do the corresponding {CH($v = 0$)} and CH* emissions (recall Figures 4, 7, and 8). The p-dependence can be understood by recognizing that [CN] is determined by the equilibrium 9: [CN] = [H] × ([HCN]/[H$_2$]) × k_{-9}/k_{+9}. [H$_2$] and [HCN] are both stable species with concentrations that scale as [H$_2$] $\sim p$ and [HCN] $\sim p^{1.5}$. The latter trend reflects the enhanced decomposition of N$_2$ with increasing p via reactions 3−5, followed by reactions 6−9. [H] scales with [H$_2$]^2, given that the main H atom production route is

$$H_2 + H_2 \rightarrow H + H + H_2 \tag{10}$$

This simple analysis predicts that [CN] will show a $p^{2.5}$ dependence, as should {CN($v = 0$)} if we ignore the small p-dependence of the plasma radius, R_{pl}.

The equilibrium 9 was also analyzed at different applied microwave powers P. At a constant pressure $p = 150$ Torr, modeling returns [HCN] $\sim P^{0.5}$ and [H] $\sim P$. [H$_2$] is essentially independent of P, and thus we predict the functional behavior [CN] $\sim P^{1.5}$. Recognizing the plasma expansion with increasing power ($R_{pl} \sim P^{0.5}$), we have {CN} $\sim P^2$, which is a little less steep than the experimentally observed dependence of {CN($v = 0$)} $\sim P^{2.5}$ (Figure 7).

4.3. Effects of Varying $F(\text{N}_2)$ and Implications for N-Doping of Diamond. The observed linear dependence of {CN($v = 0$)} and {NH($v = 0$)} on $F(\text{N}_2)$ (Figure 6) is simply a consequence of their main sources, reactions 3−8. As discussed above in the context of adding CH$_4$ to a N/H plasma, introducing N$_2$ into a C/H plasma can both change the dominant ions and introduce additional subsidiary, but relatively complex and reactive, H$_x$C$_y$N$_z^+$ ions. The observed jump in {CH($v = 0$)} at low $F(\text{N}_2)$ (also seen in Figure 6) provides indirect evidence for the appearance of such H$_x$C$_y$N$_z^+$ species. Introducing $X_0(\text{N}_2) < 0.1\%$ to a 4% CH$_4$/H$_2$ mixture cannot have a significant effect on the neutral C/H chemistry or the C$_x$H$_y$ species concentrations but, by replacing some of the dominant C$_x$H$_y^+$ ions by more complex H$_x$C$_y$N$_z^+$ ions having higher electron−ion recombination rates, could change the plasma volume, power density, or maximal gas temperature sufficiently to induce the observed jump in {CH($v = 0$)}. We have previously observed and explained a more dramatic jump in {H($n = 2$)} induced by a change in dominant ion from H$_3^+$ in a pure H$_2$ plasma to a mixture of C$_2$H$_2^+$ and C$_2$H$_3^+$ ions upon introducing CH$_4$.[44,49]

As noted in the Introduction, longstanding unresolved aspects of diamond CVD from C/N/H plasmas include the nature of the

Table 3. Calculated Gas Temperatures, T_{gas}, $[N]_{ns}/([CN]_{ns} \times 3.5)$, and $[N]_{ns}/[CH_3]_{ns}$ Concentration Ratios, $R_{inc}(N)/R_{inc}(CH_3)$ and $(R_{inc}(N)/R_{inc}(CH_3))/(X_0(N_2)/X_0(CH_4))$ Incorporation Rate Ratios, and Selected Species Concentrations (in cm^{-3}) above the Substrate Center (at $r = 0$, $z = 0.5$ mm) from Which These Ratios Are Derived for a Range of C/N/H Gas Mixtures and Process Conditions

$X_0(N_2)$ (%)	0.0001	0.002	0.01	0.6	0.6	0.6	0.6	0.6	3
$X_0(CH_4)$ (%)	4	4	4	4	4	4	4	0.4	0.4
p (Torr)	150	150	150	150	150	150	75	150	150
P (kW)	1.5	1.5	1.5	1.5	0.75	3.0	1.5	1.5	1.5
T_{gas} (K)	1402	1403	1404	1399	1399	1453	1334	1376	1363
$[N]_{ns}/([CN]_{ns} \times 3.5)$	8.16	8.30	8.05	6.75	11.9	1.23	32.0	14.8	9.57
$[N]_{ns}/[CH_3]_{ns}$	4.28×10^{-8}	8.78×10^{-7}	4.42×10^{-6}	2.32×10^{-4}	1.54×10^{-4}	1.08×10^{-3}	3.94×10^{-4}	1.34×10^{-3}	4.58×10^{-3}
$([N]_{ns}/[CH_3]_{ns})/(X_0(N_2)/X_0(CH_4))$	1.71×10^{-3}	1.76×10^{-3}	1.77×10^{-3}	1.55×10^{-3}	1.03×10^{-3}	7.20×10^{-3}	2.63×10^{-3}	8.93×10^{-4}	6.11×10^{-4}
$R_{inc}(N)/R_{inc}(CH_3)$	1.09×10^{-6}	2.24×10^{-5}	1.12×10^{-4}	5.94×10^{-3}	4.64×10^{-3}	2.39×10^{-2}	9.67×10^{-3}	3.34×10^{-2}	1.19×10^{-1}
$(R_{inc}(N)/R_{inc}(CH_3))/(X_0(N_2)/X_0(CH_4))$	4.37×10^{-2}	4.47×10^{-2}	4.48×10^{-2}	3.96×10^{-2}	3.10×10^{-2}	1.59×10^{-1}	6.44×10^{-2}	2.23×10^{-2}	1.59×10^{-2}
H	7.49×10^{15}	7.58×10^{15}	7.60×10^{15}	7.25×10^{15}	4.19×10^{15}	1.67×10^{16}	2.35×10^{15}	7.89×10^{15}	6.62×10^{15}
CH_4	4.15×10^{14}	4.10×10^{14}	4.12×10^{14}	4.45×10^{14}	6.93×10^{14}	1.55×10^{14}	3.57×10^{14}	1.54×10^{14}	2.21×10^{14}
CH_3	5.25×10^{13}	5.23×10^{13}	5.29×10^{13}	5.48×10^{13}	5.36×10^{13}	3.99×10^{13}	3.19×10^{13}	1.87×10^{13}	2.33×10^{13}
$^3CH_2$	2.67×10^{11}	2.70×10^{11}	2.74×10^{11}	2.69×10^{11}	1.57×10^{11}	4.32×10^{11}	9.50×10^{10}	1.03×10^{11}	1.05×10^{11}
$^1CH_2$	7.35×10^9	7.45×10^9	7.58×10^9	7.36×10^9	4.18×10^9	1.50×10^{10}	2.13×10^9	2.52×10^9	2.51×10^9
CH	8.96×10^9	9.16×10^9	9.31×10^9	8.73×10^9	2.96×10^9	3.21×10^{10}	2.01×10^9	3.71×10^9	3.24×10^9
C	2.88×10^{10}	2.97×10^{10}	3.00×10^{10}	2.65×10^{10}	4.77×10^9	2.35×10^{11}	3.65×10^9	2.92×10^{10}	1.92×10^{10}
$C_2(a)$	4.93×10^8	5.00×10^8	5.04×10^8	4.45×10^8	5.00×10^8	1.16×10^9	8.22×10^8	5.78×10^8	4.06×10^8
$C_2(X)$	1.50×10^7	1.55×10^7	1.61×10^7	1.45×10^7	5.67×10^6	1.38×10^8	5.27×10^6	3.47×10^6	2.77×10^6
C_2H	4.49×10^{10}	4.59×10^{10}	4.76×10^{10}	4.59×10^{10}	2.68×10^{10}	1.79×10^{11}	9.98×10^9	5.73×10^9	6.33×10^9
C_2H_2	8.10×10^{15}	8.11×10^{15}	8.31×10^{15}	8.73×10^{15}	8.81×10^{15}	9.60×10^{15}	4.91×10^{15}	1.22×10^{15}	1.77×10^{15}
C_2H_3	9.72×10^{12}	9.74×10^{12}	9.94×10^{12}	1.04×10^{13}	7.47×10^{12}	1.25×10^{13}	2.84×10^{12}	1.68×10^{12}	2.34×10^{12}
C_2H_4	2.34×10^{14}	2.32×10^{14}	2.36×10^{14}	2.58×10^{14}	2.92×10^{14}	1.33×10^{14}	7.59×10^{13}	4.05×10^{13}	6.60×10^{13}
C_2H_5	8.76×10^{10}	8.64×10^{10}	8.74×10^{10}	9.70×10^{10}	1.07×10^{11}	4.15×10^{10}	2.19×10^{10}	1.66×10^{10}	2.79×10^{10}
C_2H_6	1.61×10^{11}	1.58×10^{11}	1.59×10^{11}	1.84×10^{11}	2.94×10^{11}	3.57×10^{10}	1.19×10^{11}	2.72×10^{10}	5.29×10^{10}
C_3	3.35×10^{12}	3.44×10^{12}	3.54×10^{12}	3.44×10^{12}	6.28×10^{11}	2.50×10^{13}	7.88×10^{11}	4.39×10^{11}	4.94×10^{11}
C_3H	6.12×10^{10}	6.23×10^{10}	6.42×10^{10}	6.42×10^{10}	1.92×10^{10}	2.62×10^{11}	1.53×10^{10}	6.49×10^9	8.15×10^9
C_3H_2	7.07×10^{13}	7.11×10^{13}	7.29×10^{13}	7.66×10^{13}	3.97×10^{13}	1.28×10^{14}	2.99×10^{13}	7.31×10^{12}	1.09×10^{13}
C_4	1.69×10^5	1.75×10^5	1.85×10^5	1.75×10^5	6.47×10^4	2.00×10^6	6.68×10^4	1.02×10^4	1.02×10^4
C_4H	7.35×10^7	7.52×10^7	7.92×10^7	7.86×10^7	5.28×10^7	3.38×10^8	5.17×10^7	4.37×10^6	5.21×10^6
C_4H_2	6.23×10^{12}	6.26×10^{12}	6.56×10^{12}	7.19×10^{12}	6.83×10^{12}	9.94×10^{12}	4.28×10^{12}	1.73×10^{11}	3.37×10^{11}
$H(n=2)$	2.49×10^6	2.55×10^6	2.56×10^6	2.18×10^6	1.56×10^6	7.58×10^6	1.64×10^6	3.58×10^6	2.17×10^6
$H(n=3)$	1.37×10^5	1.40×10^5	1.41×10^5	1.19×10^5	8.61×10^4	4.22×10^5	1.16×10^5	2.13×10^5	1.25×10^5
H_2	1.02×10^{18}	1.02×10^{18}	1.02×10^{18}	1.02×10^{18}	1.02×10^{18}	9.67×10^{17}	5.34×10^{17}	1.04×10^{18}	1.03×10^{18}
N_2	4.90×10^{11}	9.82×10^{12}	5.01×10^{13}	3.18×10^{15}	3.25×10^{15}	3.38×10^{15}	1.73×10^{15}	2.94×10^{15}	2.16×10^{16}
$N_2(A3)$	5.74×10^5	1.16×10^7	5.89×10^7	3.44×10^9	4.77×10^9	3.67×10^9	6.57×10^9	5.04×10^9	3.05×10^{10}
NH_3	7.21×10^7	1.44×10^9	7.25×10^9	4.37×10^{11}	1.32×10^{12}	1.40×10^{11}	1.26×10^{12}	6.53×10^{11}	3.98×10^{12}
NH_2	8.73×10^5	1.76×10^7	8.94×10^7	5.13×10^9	9.38×10^9	3.78×10^9	8.70×10^9	7.68×10^9	3.97×10^{10}
NH	4.95×10^5	1.00×10^7	5.11×10^7	2.86×10^9	3.44×10^9	3.96×10^9	3.92×10^9	4.61×10^9	2.20×10^{10}
N	2.24×10^6	4.59×10^7	2.33×10^8	1.27×10^{10}	8.26×10^9	4.30×10^{10}	1.26×10^{10}	2.51×10^{10}	1.07×10^{11}
$CN(\times 3.5)$	2.75×10^5	5.54×10^6	2.90×10^7	1.88×10^9	6.94×10^8	3.48×10^{10}	3.93×10^8	1.70×10^9	1.12×10^{10}
HCN	4.11×10^9	8.13×10^{10}	4.21×10^{11}	2.95×10^{13}	1.83×10^{13}	1.77×10^{14}	1.16×10^{13}	2.80×10^{13}	2.36×10^{14}
H_2CN	9.58×10^4	1.90×10^6	9.80×10^6	6.76×10^8	3.10×10^8	4.65×10^9	1.93×10^8	7.38×10^8	5.92×10^9
H_2CNH	1.86×10^5	3.71×10^6	1.89×10^7	1.18×10^9	2.28×10^9	6.31×10^8	3.24×10^9	7.13×10^8	5.43×10^9
H_3CNH	1.33×10^2	2.65×10^3	1.35×10^4	8.26×10^5	1.29×10^6	3.60×10^5	1.08×10^6	5.18×10^5	3.59×10^6
H_3CNH_2	1.14×10^4	2.25×10^5	1.14×10^6	7.28×10^7	1.95×10^8	1.37×10^7	1.39×10^8	4.14×10^7	3.34×10^8
e	8.99×10^{10}	9.07×10^{10}	9.17×10^{10}	8.75×10^{10}	9.83×10^{10}	1.21×10^{11}	8.47×10^{10}	6.34×10^{10}	5.58×10^{10}
$C_2H_2^+$	6.51×10^{10}	6.56×10^{10}	6.68×10^{10}	5.90×10^{10}	6.62×10^{10}	6.62×10^{10}	5.56×10^{10}	1.50×10^{10}	8.39×10^9
$C_2H_3^+$	2.48×10^{10}	2.49×10^{10}	2.44×10^{10}	9.35×10^9	1.20×10^{10}	2.72×10^9	1.62×10^{10}	1.32×10^{10}	5.84×10^8
H_3^+	1.82×10^7	1.84×10^7	1.77×10^7	7.90×10^6	9.96×10^6	5.93×10^6	1.57×10^7	9.71×10^7	1.34×10^7
H_2^+	2.52×10^4	2.56×10^4	2.55×10^4	2.20×10^4	2.85×10^4	3.42×10^4	7.60×10^4	4.20×10^4	2.68×10^4
N_2H^+	6.35×10^1	1.29×10^3	6.32×10^3	1.80×10^5	2.31×10^5	1.38×10^5	4.03×10^5	2.08×10^6	2.15×10^6
NH_4^+	6.90×10^5	1.38×10^7	6.97×10^7	3.58×10^9	9.11×10^9	1.95×10^9	6.02×10^9	5.41×10^9	1.81×10^{10}
$HCNH^+$	4.07×10^6	8.07×10^7	4.09×10^8	1.56×10^{10}	1.10×10^{10}	4.96×10^{10}	6.89×10^9	2.97×10^{10}	2.88×10^{10}

gas-phase precursor(s) responsible for N-doping and the cause of the growth rate enhancement upon small (even down to the level of a few ppm) additions of N_2 to the process gas.[5−7,9−15] The current study directly addresses the first of these questions. Table 3 presents calculated species number densities just above the substrate center ($r = 0$, $z = 0.5$ mm) for four different N_2 input mole fractions (1, 20, 100, and 6000 ppm) under otherwise base conditions and for two other values of P (0.75 and 3 kW) and one

other value of p (75 Torr) with the base, 0.6% N_2/4% CH_4/H_2 mixture. Two other C/N/H gas mixtures are also considered for which the input N mole fraction (0.6% and 3% N_2, respectively) exceeds that of C (0.4% CH_4), again with the balance being H_2 and at base conditions of P and p. The values reported in Table 3 are the raw model outputs, apart from the case of CN, where the values have been increased by the empirical factor $b \approx 3.5$. Of the directly incorporable N-containing species included in the model, N, NH, NH_2, and CN, atomic nitrogen is the most abundant close to the diamond surface under base P and p, and the near-surface N atom number densities, $[N]_{ns}$, returned by the modeling are typically an order of magnitude higher than $[CN]_{ns}$. However, $[CN]_{ns}$ increases more rapidly than $[N]_{ns}$ upon increasing P or p, so that the predicted $[N]_{ns}/[CN]_{ns}$ ratio shows a $\approx$5-fold decrease upon doubling p from 75 to 150 Torr or P from 1.5 to 3 kW. This trend suggests that gas–surface reactions involving CN may become an increasingly important route to incorporating N within diamond grown at high P and p.

The near-surface species concentrations returned by the plasma modeling are necessary but not sufficient information for estimating the relative contributions different species make to diamond growth. This determination is also sensitive to the relative sticking coefficients, γ, of the various species at a growing diamond surface. These quantities, and their variation with process conditions, are still not well characterized however. Prior molecular dynamics simulations of CH_x ($x = 0-3$) encounters with diamond (100) and (111) surfaces at temperatures relevant to diamond CVD found that sticking is more probable if the incident species has more free electrons and fewer H atoms:[59] for example, C atoms were predicted to have an order of magnitude higher sticking probability than CH_3 radicals. The present modeling assumes a net sticking probability for CH_3 radicals that has been derived by comparing near-surface gas-phase model outputs with experimentally measured growth rates,[60] while the sticking coefficients for other small, potentially reactive radical species (CH_2, CH, C, NH_2, NH, N, and CN) were all set at 0.1. This latter value is based on the assumptions that these species each have unit incorporation probability at a non-H-terminated surface radical site (henceforth C_s^*), and that the calculated steady-state fraction $X(C_s^*)$ of such sites at base growth conditions is $X(C_s^*) \sim 0.1$.[60] These sticking probabilities are thus $\approx$25 times greater than that derived for CH_3 radicals under the present base conditions, but since $[CH_2]_{ns}$, $[CH]_{ns}$ and $[C]_{ns}$ are all much lower than $[CH_3]_{ns}$ (Table 3), even with their much higher assumed net incorporation probabilities $\sim X(C_s^*)$, these species are still predicted to make little contribution to the overall growth rate. Furthermore, the rates R_{+9} and R_{-9} are so high that $[CN]_{ns}$ is rather insensitive to the choice of γ_{CN}. However, the situation with the remaining species, and especially N atoms, is less clear. Given the choice of what is essentially an upper-limit value of γ_N, the ratios of the net incorporation rates $(R_{inc}(N)/R_{inc}(CH_3) \sim (\gamma_{inc}(N) \times [N]_{ns})/(\gamma_{inc}(CH_3) \times [CH_3]_{ns}))$ reported in Table 3 should definitely also be taken as upper limits.

The only difference in the input parameters for the data listed in the first four columns of Table 3 is the value of $X_0(N_2)$. The predicted value of $[N]_{ns}/[CH_3]_{ns}$ increases from $\approx 4 \times 10^{-8}$ for $X_0(N_2) = 0.0001\%$ (1 ppm) to 9×10^{-7} for $X_0(N_2) = 0.002\%$, 4.4 $\times 10^{-6}$ when $X_0(N_2) = 0.01\%$, and 2.3×10^{-4} for $X_0(N_2) = 0.6\%$. These are each much smaller than the respective $X_0(N_2)/X_0(CH_4)$ ratios in the input source gas mixtures, but the ratio of these ratios, the "relative nitrogen activation fraction" $([N]_{ns}/[CH_3]_{ns})/(X_0(N_2)/X_0(CH_4))$, is consistently $(1.6 \pm 0.1) \times 10^{-3}$.

The absolute value of the activation fraction will be process-dependent, but for small $X_0(N_2)$ and an otherwise consistent set of process conditions, the $[N]_{ns}/[CH_3]_{ns}$ ratio varies essentially proportionally with input $X_0(N_2)$. As Table 3 shows, doubling P from 1.5 to 3 kW is predicted to result in a $\approx$5-fold increase in relative nitrogen activation, which may have a yet larger impact on the relative N/C incorporation efficiency given the decrease in $[N]_{ns}/[CN]_{ns}$ that also accompanies such an increase in P. However, that the activation fraction is always $\ll 1$ and the ratio of ratios $(R_{inc}(N)/R_{inc}(CH_3))/(X_0(N_2)/X_0(CH_4))$ (i.e., the normalized incorporation rate) is fairly constant across a broad range of nitrogen input fractions and consistently <1, should offer a useful guide when it comes to predicting N concentrations and N incorporation efficiencies in CVD diamond.

Finally, it is instructive to compare the present findings with the predictions of the one previous modeling study of a MW-activated C/N/H plasma operating at pressures and temperatures relevant to diamond CVD, by Yamada.[30] The earlier work treated the following conditions: $F(CH_4) = 25$ sccm, $F(N_2) = 2.5$ sccm, $F(H_2) = 500$ sccm (i.e., $X_0(CH_4) = 4.7\%$ and $X_0(N_2) = 0.47\%$), $p = 120$ Torr, and $P = 3$ kW into a plasma volume seemingly about twice that of the present work. The calculated maximum gas temperature in the hot plasma core was $T_{max} \approx 3000$ K and the near-substrate gas temperature $T_{gas} \approx 1500$ K. These temperatures are a little higher than found from the present modeling, while the pressure is a little lower. Differences between the earlier data and that shown in the fourth column of Table 3 are generally minor: $[NH_3]_{ns}$ is here about 1 order of magnitude larger than in the earlier work, even after correcting for the difference in pressure, but the $[NH]_{ns}$ and $[N]_{ns}$ values agree between the two studies to within a factor of 2. Our higher $[NH_3]_{ns}$ can be traced to the role of reactions 2 and 3 in providing a nonthermal route to activating and dissociating N_2, which was not considered in the earlier modeling, while the lower $[N]_{ns}$ is likely due to our high assumed value of γ_N. Importantly, the relative nitrogen activation fraction ($\approx 6.7 \times 10^{-3}$) found by Yamada[30] is not very different from ours, highlighting the predominant roles of thermal chemistry and transport in determining the near-substrate species concentrations.

5. CONCLUSIONS

Spatially resolved optical emission and line-of-sight absorption spectroscopy methods have been used to probe selected atomic (H), radical (CH, C_2, CN, and NH), and triplet N_2 molecule densities in MW-activated CH_4/N_2/H_2 gas mixtures such as are used in diamond CVD, as functions of the source gas mole fractions, total pressure, and applied MW power. These data have been rationalized using complementary 2-D (r, z) coupled kinetic and transport modeling, which succeeds, mostly quantitatively, in reproducing all of the measured trends in species column densities and OES intensities. After calibration against experiment, the model was run over a wider range of N/C input ratios, $2.5 \times 10^{-5} \leq X_0(N_2)/X_0(CH_4) \leq 7.5$, than could be explored experimentally, as well as with a higher MW power of 3 kW.

Key findings include the following:

(i) For base conditions of $p = 150$ Torr and $P = 1.5$ kW, strongly bound N_2 molecules constitute >99.75% of the total nitrogen content in the reactor, falling only to $\approx$99.5% even in the hot plasma core. Less than 0.25% of the supplied nitrogen becomes HCN, with all other N-

containing species two or more orders of magnitude less abundant still.

(ii) Two reaction sequences enable N_2 to participate in the plasma chemistry. Reaction 4, proposed as the dominant source of N atoms in the one previous modeling study of a MW-activated C/N/H plasma,[30] involves the reaction of N_2 with CH radicals. Reactions 2 and 3, identified in our recent studies of MW-activated N_2/H_2 plasmas,[29] involve electron impact excitation of N_2 in the hot plasma region, energy pooling in the metastable $N_2(A^3\Sigma_u^+)$ state, and subsequent reaction with H atoms. The former pathway is the more important route to forming N atoms at higher gas pressures, input powers, or CH_4 input fractions.

(iii) Of the N-containing species that can be considered potentially reactive at the growing diamond surface, namely, N, NH, NH_2, and CN, the near-surface gas-phase number density of atomic nitrogen under base conditions is higher than $[NH]_{ns}$ or $[NH_2]_{ns}$ and typically an order of magnitude higher than $[CN]_{ns}$.

(iv) Comparing the measured $\{CN(\nu = 0)\}$ data with model predictions reveals an underestimation that hints at an unusual (for high pressures, $p > 100$ Torr) nonthermal vibrational population distribution in HCN molecules formed in the fast exothermic reaction 9 and significantly enhanced rates for subsequent reactions involving these "hot" HCN molecules.

(v) Changing the input N/C ratio in the process gas mixture under base conditions causes a proportional change in the $[N]_{ns}/[CH_3]_{ns}$ ratio but has little effect on the $[N]_{ns}/[NH]_{ns}/[CN]_{ns}$ ratios just above the growing surface. The $[N]_{ns}/[CH_3]_{ns}$ ratio is consistently much smaller than the $X_0(N_2)/X_0(CH_4)$ ratio in the input gas mixture, reflecting the stability of N_2 under these process conditions. Increasing p or P promotes N_2 dissociation and so raises both the $[N]_{ns}/[CH_3]_{ns}$ and $[CN]_{ns}/[CH_3]_{ns}$ ratios for the same N input fraction.

Finally, we return briefly to consider the longstanding issue raised in the Introduction: how the presence of small amounts of nitrogen in the gas phase leads to an increase in diamond growth rate and influences the surface morphology. H atoms and CH_3 radicals are generally accepted as the key species driving diamond CVD from MW-activated gas mixtures. As Table 3 shows, increasing $X_0(N_2)$ from 1 to 20 ppm has no perceptible effect on the $[H]_{ns}$ or $[CH_3]_{ns}$ values. Even at $X_0(N_2) = 100$ ppm, $[CH_3]_{ns}$ increases by little more than 1%. Clearly, the present analysis confirms that trace additions of N_2 (a rather inert species) have very little impact on the C/H chemistry or on $[H]$ or $[CH_3]$ close to the growing diamond surface. N atoms and NH and CN radicals will all be present in the near-surface volume, but for $X_0(N_2) = 100$ ppm, their number densities will be some 5–6 orders of magnitude smaller than $[CH_3]_{ns}$. Because of the small relative nitrogen activation fraction, this is some three orders less than the $X_0(N_2)/X_0(CH_4)$ ratio, although this disparity in nitrogen activation versus methane may be partially compensated by the higher (assumed) incorporation efficiency of N atoms versus CH_3 radicals at the growing diamond surface. Increasing p or P produces an obvious increase in $[CN]_{ns}$ relative to $[NH_x]_{ns}$ ($x = 0-2$), so we also recognize that different gas–surface chemistry could drive N incorporation under conditions of low and high gas activation. Energetically feasible reaction sequences providing for N, NH, or CN to be accommodated on a model diamond (100) surface have been identified, and are described in a companion paper,[61] but it is hard to imagine that such rare encounters could directly account for the observed rate enhancements or morphological changes. It is also widely accepted that these N-induced effects are just one factor in a multiparameter growth space, so that the result of adding N_2 to the process mixture also depends on the substrate condition and its temperature during growth.[14] Hence, the present study tends to support prior suggestions that the key role of trace N incorporation is in locally chemically activating the diamond surface or otherwise enabling faster growth at high substrate temperature by somehow limiting strain[62] or nonepitaxial growth[14] in the resulting material that would typically result under such conditions. An additional effect of incorporated nitrogen could arise if the migration of an NH surface group along the diamond surface is significantly hindered relative to that of CH_2. Such immobile NH groups could then serve as anchors for migrating CH_2 groups (as does the step edge in regular step-flow growth), thus enhancing formation of difficult-to-etch chains of CH_2 surface bridges. This decrease in the average migration length of CH_2 groups before incorporation would reduce the rate at which they are etched and thus accelerate diamond growth.

All underlying experimental data is openly available under the DOI: 10.5523/bris.rjq1btqricc717ltaele2yfu4.

■ AUTHOR INFORMATION

Corresponding Authors
*M.N.R.A. E-mail: mike.ashfold@bris.ac.uk. Tel: +44 (117) 9288312.
*Yu.A.M. E-mail: ymankelevich@mics.msu.su.

Notes
The authors declare no competing financial interest.

■ REFERENCES

(1) Mainwood, A. In *CVD Diamond for Electronic Sensors and Devices*; Sussmann, R. S., Ed.; Wiley: Chichester, U.K., 2009; Chapter 4.

(2) Li, B. B.; Tosin, M. C.; Peterlevitz, A. C.; Baranauskas, V. Measurement of the Substitutional Nitrogen Activation Energy in Diamond Films. *Appl. Phys. Lett.* **1998**, 73, 812−814.

(3) Tallaire, A.; Collins, A. T.; Charles, D.; Achard, J.; Sussmann, R.; Gicquel, A.; Newton, M. E.; Edmonds, A. M.; Cruddace, R. J. Characterisation of High Quality Thick Single-Crystal Diamond Grown by CVD with a Low Nitrogen Addition. *Diamond Relat. Mater.* **2006**, 15, 1700−1707.

(4) Webster, S.; Chen, Y.; Turri, G.; Bennett, A.; Wickham, B.; Bass, M. Intrinsic and Extrinsic Absorption of CVD Single Crystal Diamond from the Middle Ultraviolet to the Far Infrared. *J. Opt. Soc. Am. B* **2015**, 32, 479−484.

(5) Jin, S.; Moustakas, T. D. Effect of Nitrogen on the Growth of Diamond Films. *Appl. Phys. Lett.* **1994**, 65, 403−405.

(6) Müller-Sebert, W.; Wörner, E.; Fuchs, F.; Wild, C.; Koidl, P. Nitrogen Induced Increase of Growth Rate in Chemical Vapor Deposition of Diamond. *Appl. Phys. Lett.* **1996**, 68, 759−760.

(7) Yan, C.-S.; Vohra, Y. K.; Mao, H.-K.; Hemley, R. J. Very High Growth Rate Chemical Vapour Deposition of Single-Crystal Diamond. *Proc. Natl. Acad. Sci. U. S. A.* **2002**, *99*, 12523−12525.

(8) Chayahara, A.; Mokuno, Y.; Horino, Y.; Takasu, Y.; Kato, H.; Yoshikawa, H.; Fujimori, N. The Effect of Nitrogen Addition during High-rate Homoepitaxial Growth of Diamond by Microwave Plasma CVD. *Diamond Relat. Mater.* **2004**, *13*, 1954−1958.

(9) Liu, Y.; Raabe, D. Influence of Nitrogen Doping on Growth Rate and Texture Evolution of Chemical Vapor Deposition Thin Films. *Appl. Phys. Lett.* **2009**, *94*, 021119.

(10) Achard, J.; Silva, F.; Brinza, O.; Tallaire, A.; Gicquel, A. Coupled Effect of Nitrogen Addition and Surface Temperature on the Morphology and the Kinetics of Thick CVD Diamond Single Crystals. *Diamond Relat. Mater.* **2007**, *16*, 685−689.

(11) Dunst, S.; Sternschulte, H.; Schreck, M. Growth Rate Enhancement by Nitrogen in Diamond Chemical Vapor Deposition — a Catalytic Effect. *Appl. Phys. Lett.* **2009**, *94*, 224101.

(12) Lu, J.; Gu, Y.; Grotjohn, T. A.; Schuelke, T.; Asmussen, J. Experimentally Defining the Safe and Efficient, High Pressure Microwave Plasma Assisted CVD Operating Regime for Single Crystal Diamond Synthesis. *Diamond Relat. Mater.* **2013**, *37*, 17−28.

(13) Bogdanov, S.; Vikharev, A.; Gorbachev, A.; Muchnikov, A.; Radishev, D.; Ovechkin, N.; Parshin, V. Growth-rate Enhancement of High-quality, Low-loss CVD-produced Diamond Disks Grown for Microwave Windows Application. *Chem. Vap. Deposition* **2014**, *20*, 32−38.

(14) Yamada, H.; Chayahara, A.; Mokuno, Y. Effects of Intentionally Introduced Nitrogen and Substrate Temperature on Growth of Diamond Bulk Single Crystals. *Jpn. J. Appl. Phys.* **2016**, *55*, 01AC07 and references therein.

(15) Locher, R.; Wild, C.; Herres, N.; Behr, D.; Koidl, P. Nitrogen Stabilized 100 Texture in Chemical Vapour Deposited Diamond Films. *Appl. Phys. Lett.* **1994**, *65*, 34−36.

(16) Cao, G. Z.; Schermer, J. J.; van Enckevort, W. J. P.; Elst, W. A. L. M.; Giling, L. J. Growth of {100} Textured Diamond Films by the Addition of Nitrogen. *J. Appl. Phys.* **1996**, *79*, 1357−1364.

(17) Avigal, Y.; Glozman, O.; Etsion, I.; Halperin, G.; Hoffman, A. [100]-Textured Diamond Films for Tribological Applications. *Diamond Relat. Mater.* **1997**, *6*, 381−385.

(18) Tang, C. J.; Fernandes, A. J. S.; Costa, F.; Pinto, J. L. Effect of Microwave Power and Nitrogen Addition on the Formation of {100} Faceted Diamond from Microcrystalline to Nanocrystalline. *Vacuum* **2011**, *85*, 1130−1134.

(19) Achard, J.; Silva, F.; Tallaire, A.; Bonnin, X.; Lombardi, G.; Hassouni, K.; Gicquel, A. High Quality MPACVD Diamond Single Crystal Growth: High Microwave Power Density Regime. *J. Phys. D: Appl. Phys.* **2007**, *40*, 6175−6188.

(20) Vandevelde, T.; Wu, T. D.; Quaeyhaegens, C.; Vlekken, J.; D'Olieslaeger, M.; Stals, L. Correlation Between the OES Plasma Composoton and the Diamond Film Properties During Microwave PA-CVD with Nitrogen Addition. *Thin Solid Films* **1999**, *1−2*, 159−163.

(21) Yan, C.-S.; Vohra, Y. K. Multiple Twinning and Nitrogen Defect Center in Chemical Vapour Deposited Homoepitaxial Diamond. *Diamond Relat. Mater.* **1999**, *8*, 2022−2031.

(22) Dandy, D. S. Influence of the Gas Phase on Doping in Diamond Chemical Vapor Deposition. *Thin Solid Films* **2001**, *381*, 1−5.

(23) Butler, J. E.; Oleynik, I. A Mechanism for Crystal Twinning in the Growth of Diamond by Chemical Vapour Deposition. *Philos. Trans. R. Soc., A* **2008**, *366*, 295−311.

(24) Regemorter, T. V.; Larsson, K. Effect of Coadsorbed Dopants on Diamond Initial Growth Processes: CH₃ Adsorption. *J. Phys. Chem. A* **2008**, *112*, 5429−5435.

(25) Regemorter, T. V.; Larsson, K. Effect of a NH Coadsorbate on the CH₃ (or CH₂) Adsorption to a Surface Step on Diamond (100). *J. Phys. Chem. C* **2009**, *113*, 19891−19896.

(26) Butler, J. E.; Mankelevich, Yu.A.; Cheesman, A.; Ma, J.; Ashfold, M. N. R. Understanding the Chemical Vapor Deposition of Diamond: Recent Progress. *J. Phys.: Condens. Matter* **2009**, *21*, 364201 and references therein.

(27) Van Regemorter, T.; Larsson, K. Effect of Substitutional N on Important Chemical Vapor Deposition Growth Steps. *J. Phys. Chem. A* **2009**, *113*, 3274−3284.

(28) Yiming, Z.; Larsson, F.; Larsson, K. Effect of CVD Diamond Growth by Doping with Nitrogen. *Theor. Chem. Acc.* **2014**, *133*, 1432.

(29) Truscott, B. S.; Kelly, M. W.; Potter, K. J.; Johnson, M.; Ashfold, M. N. R.; Mankelevich, Yu.A. Microwave Plasma-Activated Chemical Vapour Deposition of Nitrogen-Doped Diamond, I: N₂/H₂ and NH₃/H₂ Plasmas. *J. Phys. Chem. A* **2015**, *119*, 12962−12976.

(30) Yamada, H. Numerical Simulations to Study Growth of Single-Crystal Diamond by Using Microwave Plasma Chemical Vapor Deposition with Reactive (H, C, N) Species. *Jpn. J. Appl. Phys.* **2012**, *51*, 090105.

(31) Kramida, A.; Ralchenko, Yu.; Reader, J.; NIST ASD Team. *NIST Atomic Spectra Database*, version 5.2; National Institute of Standards and Technology: Gaithersburg, MD, 2014. Available at http://physics.nist.gov/asd (accessed on April 28, 2015).

(32) Brazier, C. R.; Ram, R. S.; Bernath, P. F. Fourier Transform Spectroscopy of the A³Π−X³Σ⁻ Transition of NH. *J. Mol. Spectrosc.* **1986**, *120*, 381−402.

(33) Kirby, K. P.; Goldfield, E. M. Theoretical Study of the Radiative Properties of the Triplet States of the NH Radical: Transition Dipole Moments, Radiative Lifetimes, Photodissociation Cross sections. *J. Chem. Phys.* **1991**, *94*, 1271−1276.

(34) Owono Owono, L. C.; Ben Abdallah, D.; Jaidane, N.; Ben Lakhdar, Z. Theoretical Radiative Properties Between States of the Triplet Manifold of NH Radical. *J. Chem. Phys.* **2008**, *128*, 084309.

(35) Zachwieja, M. New Investigations of the A²Δ−X²Π Band System in the CH Radical and a New Reduction of the Vibration-Rotation Spectrum of CH from the Atmos Spectra. *J. Mol. Spectrosc.* **1995**, *170*, 285−309.

(36) Wills, J. B.; Smith, J. A.; Boxford, W. E.; Elks, J. M. F.; Ashfold, M. N. R.; Orr-Ewing, A. J. Measurements of C₂ and CH Concentrations and Temperatures in a DC Arc Jet using Cavity Ring Down Spectroscopy. *J. Appl. Phys.* **2002**, *92*, 4213−4222 and references therein.

(37) Bernath, P. F.; Brazier, C. R.; Olsen, T.; Hailey, R.; Fernando, W. T. M. L.; et al. Spectroscopy of the CH Free Radical. *J. Mol. Spectrosc.* **1991**, *147*, 16−26.

(38) Garland, N. L.; Crosley, D. R. Relative Transition Probability Measurements in the A−X and B−X Systems of CH. *J. Quant. Spectrosc. Radiat. Transfer* **1985**, *33*, 591−595.

(39) Lloyd, G. M.; Ewart, P. High Resolution Spectroscopy and Spectral Simulation of C₂ using Degenerate Four-Wave Mixing. *J. Chem. Phys.* **1999**, *110*, 385−392.

(40) Ram, R. S.; Davis, S. P.; Wallace, L.; Engleman, R.; Appadoo, D. R. T.; Bernath, P. F. Fourier Transform Emission Spectroscopy of the B²Σ⁺−X²Σ⁺ System of CN. *J. Mol. Spectrosc.* **2006**, *237*, 225−231.

(41) Knowles, P. J.; Werner, H.-J.; Hay, P. J.; Cartwright, D. C. The A²Π−X²Σ⁺ Red and B²Σ⁺−X²Σ⁺ Violet Systems of the CN Radical: Accurate Multireference Configuration Interaction Calculations of the Radiative Transition Probabilities. *J. Chem. Phys.* **1988**, *89*, 7334−7343.

(42) Roux, F.; Michaud, F.; Vervloet, M. High-Resolution Fourier Spectrometry of ¹⁴N₂ Violet Emission Spectrum: Extensive Analysis of the C³Πᵤ→B³Πᵧ System. *J. Mol. Spectrosc.* **1993**, *158*, 270−277.

(43) Gilmore, F. R.; Laher, R. R.; Espy, P. J. Franck-Condon Factors, r-Centroids, Electronic Transition Moments, and Einstein Coefficients for Many Nitrogen and Oxygen Band Systems. *J. Phys. Chem. Ref. Data* **1992**, *21*, 1005−1107.

(44) Ma, J.; Richley, J. C.; Ashfold, M. N. R.; Mankelevich, Yu.A. Probing the Plasma Chemistry in a Microwave Reactor used for Diamond Chemical Vapour Deposition by Cavity Ring Down Spectroscopy. *J. Appl. Phys.* **2008**, *104*, 103305.

(45) Ma, J.; Ashfold, M. N. R.; Mankelevich, Y. A. Validating Optical Emission Spectroscopy as a Diagnostic of Microwave Activated CH₄/Ar/H₂ Plasmas used for Diamond Chemical Vapor Deposition. *J. Appl. Phys.* **2009**, *105*, 043302.

(46) Western, C. M. *PGOPHER, A Program for Rotational, Vibrational and Electronic Spectra*, version 9.0; University of Bristol, 2015. Available at http://pgopher.chm.bris.ac.uk/.

(47) Stolk, R. L.; ter Meulen, J. J. Cavity Ring Down Spectroscopy Measurements of Absolute CN Concentrations During Flame Deposition of Diamond. *J. Chem. Phys.* **2002**, *117*, 8281−8291.

(48) Luque, J.; Jeffries, J. B.; Smith, G. P.; Crosley, D. R.; Scherer, J. J. Combined Cavity Ringdown Absorption and Laser-Induced Fluorescence Imaging Measurements of CN(B−X) and CH(B−X) in Low-Pressure CH_4−O_2−N_2 and CH_4−NO−O_2−N_2 Flames. *Combust. Flame* **2001**, *126*, 1725−1735.

(49) Mankelevich, Yu.A.; Ashfold, M. N. R.; Ma, J. Plasma-chemical Processes in Microwave Plasma Enhanced Chemical Vapour Deposition Reactors Operating with C/H/Ar Gas Mixtures. *J. Appl. Phys.* **2008**, *104*, 113304.

(50) Smith, G. P.; Golden, D. M.; Frenklach, M.; Moriarty, N. W.; Eiteneer, B.; Goldenburg, M.; Bowman, C. T.; Hanson, R. K.; Song, S.; Gardiner, W. C., Jr.; Lissianski, V. V.; Qin, Z. W. *GRI-Mech 3.0*. Available at http://www.me.berkeley.edu/gri_mech/ (accessed 2016).

(51) Smith, J. A.; Wills, J. B.; Moores, H. S.; Orr-Ewing, A. J.; Ashfold, M. N. R.; Mankelevich, Yu.A.; Suetin, N. V. Effects of NH_3 and N_2 Additions to Hot Filament Activated CH_4/H_2 Gas Mixtures. *J. Appl. Phys.* **2002**, *92*, 672−681.

(52) Dean, A. M.; Bozzelli, J. W. Combustion Chemistry of Nitrogen. In *Gas-Phase Combustion Chemistry*; Gardiner, W. C., Jr., Ed.; Springer: New York, 2000.

(53) Yelle, R. V.; Vuitton, V.; Lavvas, P.; Klippenstein, S. J.; Smith, M. A.; Hörst, S. M.; Cui, J. Formation of NH_3 and CH_2NH in Titan's Upper Atmosphere. *Faraday Discuss.* **2010**, *147*, 31.

(54) Itikawa, Y. Cross Sections for Electron Collisions with Nitrogen Containing Molecules. *J. Phys. Chem. Ref. Data* **2006**, *35*, 31−53.

(55) Janev, R. K.; Reiter, D. Collision Processes of $C_{2,3}H_y$ and $C_{2,3}H_y^+$ Hydrocarbons with Electrons and Protons. *Phys. Plasmas* **2004**, *11*, 780−829.

(56) Millar, T. J.; Farquhar, P. R. A.; Willacy, P. K. The UMIST Database for Astrochemistry 1995. *Astron. Astrophys., Suppl. Ser.* **1997**, *121*, 139−185.

(57) Bethardy, G. A.; Northrup, F. J.; He, G.; Tokue, I.; Macdonald, R. G. Initial Vibrational Level Distribution of $HCN[X^1\Sigma^+(v_1 0 v_3)]$ from the $CN(X^2\Sigma^+)$ + H_2 → HCN + H Reaction. *J. Chem. Phys.* **1998**, *109*, 4224−4236.

(58) Cannon, B. D.; Francisco, J. S.; Smith, I. W. M. The Relaxation of HCN(101) by V-T,R and V-V Energy Transfer. *Chem. Phys.* **1984**, *89*, 141−150.

(59) Eckert, M.; Neyts, E.; Bogaerts, A. On the Reaction Behaviour of Hydrocarbon Species at Diamond (100) and (111) Surfaces: a Molecular Dynamics Investigation. *J. Phys. D: Appl. Phys.* **2008**, *41*, 032006.

(60) May, P. W.; Ashfold, M. N. R.; Mankelevich, Yu.A. Microcrystalline, Nanocrystalline, and Ultrananocrystalline Diamond Chemical Vapor Deposition: experiment and Modelling of the Factors Controlling Growth Rate, Nucleation, and Crystal Size. *J. Appl. Phys.* **2007**, *101*, 053115.

(61) Kelly, M. W.; Halliwell, S. C.; Pattle, J. D.; Harvey, J. N.; Ashfold, M. N. R. Theoretical Investigations of the Reactions of N and O Containing Species on a Diamond 2 × 1-Reconstructed (100) Surface. *J. Phys. Chem. A* **2016**, submitted for publication.

(62) Mokuno, Y.; Kato, Y.; Tsubouchi, N.; Chayahara, A.; Yamada, H.; Shikata, S. A Nitrogen Doped Low-dislocation Density Free-standing Single Crystal Diamond Plate Fabricated by a Lift-off Process. *Appl. Phys. Lett.* **2014**, *104*, 252109.